

Strong Electronic Interaction of Amorphous Fe₂O₃ Nanosheets with Single-Atom Pt toward Enhanced Carbon Monoxide Oxidation

Wenlong Chen, Yanling Ma, Fan Li, Lei Pan, Wenpei Gao, Qian Xiang, Wen Shang, Chengyi Song, Peng Tao, Hong Zhu, Xiaoqing Pan, Tao Deng, and Jianbo Wu*

Platinum-based catalysts are critical to several chemical processes, but their efficiency is not satisfying enough in some cases, because only the surface active-site atoms participate in the reaction. Henceforth, catalysts with single-atom dispersions are highly desirable to maximize their mass efficiency, but fabricating these structures using a controllable method is still challenging. Most previous studies have focused on crystalline materials. However, amorphous materials may have enhanced performance due to their distorted and isotropic nature with numerous defects. Here reported is the facile synthesis of an atomically dispersed catalyst that consists of single Pt atoms and amorphous Fe₂O₃ nanosheets. Rational control can regulate the morphology from single atom clusters to sub-nanoparticles. Density functional theory calculations show the synergistic effect resulted from the strong binding and stabilization of single Pt atoms with the strong metal-support interaction between the in situ locally anchored Pt atoms and Fe₂O₃ lead to a weak CO adsorption. Moreover, the distorted amorphous Fe₂O₃ with O vacancies is beneficial for the activation of O₂, which further facilitates CO oxidation on nearby Pt sites or interface sites between Pt and Fe₂O₃, resulting in the extremely high performance for CO oxidation of the atomic catalyst.

1. Introduction


In nowadays, catalysts have showed critical role for industrial and energy fields. Among the catalysts, the Pt has been proved one of the most widely used and most efficient materials. Supported metal nanostructures are the most widely used type of heterogenous catalyst in industrial processes, especially for the Pt-based ones. However, the high cost of Pt noble metal has limited its industrial applications. The size of catalyst plays an important role for the catalytic reactions and can make a huge difference of performance even the component of catalysts is the same. For the supported metal nanostructures, enormous efforts have contributed to improving the performance of supported metal catalysts by controlling the size of metal particles. However, for the most widely studied work, the usage of noble metals is still very high and, on the other hand, the utilization efficiency of noble metals in these supported catalysts is far less than satisfactory. Recent reports have

demonstrated that sub-nanoclusters could have better catalytic performance and selectivity than the traditional nanometer-scale particles.^[1] Low-coordinated and unsaturated atoms often act as active sites,^[2] henceforth it is highly reasonable to downsize the particles or clusters to more dispersed single atoms in order to make use of each metal atom to achieve desirable catalysts for catalytic reactions. With this strategy in mind, it has called great interesting for the exploration of single-atom catalysts in the past several years since 2011,^[1a] especially in nowadays. Till now, several kinds of single-atom catalysts on substrates have been fabricated, such as Pt₁/FeO_x,^[1a,b] Pt/θ-Al₂O₃,^[3,4] Au/CeO₂,^[5] Pd/TiO₂,^[6] Pt/CeO₂, Pd/Ru, Ir₁/FeO_x,^[7] Au₁/FeO_x, Co/NG, Pt/Fe-N-C,^[8] Pt/ZTC,^[9] Pt/Graphene,^[1c,10] Pt-CN,^[11] Pt/TiN,^[12] Pt/carbon,^[13] Fe-N_x,^[14] Rh/CoO.^[15] Although the single-atom catalysts have shown attractive performances, wide employment is still hampered mainly due to the lack of readily available synthetic approaches with facile controllable methods and ultra-low loading (usually below 0.5%).^[6,16] Also, the most attention was focused on the single-atom elements components, which were however supported in pre-prepared crystallized substrates.

W. Chen, Y. Ma, F. Li, L. Pan, Q. Xiang, Prof. W. Shang, Prof. C. Song, Prof. P. Tao, Prof. T. Deng, Prof. J. Wu
State Key Laboratory of Metal Matrix Composites
School of Materials Science and Engineering
Shanghai Jiao Tong University
800 Dongchuan Road, Shanghai 200240, P. R. China
E-mail: jianbowu@sjtu.edu.cn

Dr. W. Gao, Prof. X. Pan
Department of Chemical Engineering and Materials Science
University of California
Irvine, CA 92697, USA

Prof. H. Zhu
University of Michigan – Shanghai Jiao Tong University Joint Institute
Shanghai Jiao Tong University
800 Dongchuan Road, Shanghai 200240, P. R. China
Prof. T. Deng, Prof. J. Wu
Center of Hydrogen Science
Shanghai Jiao Tong University
800 Dongchuan Road, Shanghai 200240, P. R. China

 The ORCID identification number(s) for the author(s) of this article can be found under <https://doi.org/10.1002/adfm.201904278>.

DOI: 10.1002/adfm.201904278

There is still very limited study to explore the roles of supports materials compared to the metal single-atoms ingredients.

Crystalline catalysts or supports have been widely studied in the last decade's years.^[1a,b,d,15,17] However, their amorphous structures are still needed to be focused due to their unique structures and characteristics in many fields. For example, since the catalytic process for CO oxidation involves the participation of the supports, the number and activity of these supports active centers would be important factors for the catalytic performance. A distorted structure material would likely provide more such active sites, and an amorphous structured-material surface may possess more oxygen vacancy which is beneficial for the CO oxidation process.^[18] In light of this, amorphous oxides supports, which own much more distorted structure than crystalline ones, are able to possess higher catalytic activity for CO oxidation reaction. Furthermore, amorphous materials possess highly homogenous sites within a solid mixture down to the atomic scale, isotropic molecular diffusion, and more percolation pathways, providing open framework and fast species diffusion.^[18b,19]

Here, we reported a facile method for the preparation of highly dispersed Pt single-atom catalysts on amorphous Fe₂O₃ 2D nanosheet substrates (Pt-SA/A-Fe₂O₃). The composites could be further precisely controlled from single atom, co-exist of single atom with sub-nanoatoms clusters (Pt-SC/A-Fe₂O₃), to sub-nano nanoparticles Pt on Fe₂O₃ 2D nanosheets (Pt-SN/A-Fe₂O₃) by different loading contents of Pt. We studied the synergistic influence between different size Pt and the amorphous Fe₂O₃ support on the efficiency of CO conversion. The Pt-SA/A-Fe₂O₃ catalyst showed extremely high activity for CO oxidation reactions, turning out to be the most active catalysts, with a low temperature around 70 °C to achieve 100% CO conversion efficiency in comparison with the counterparts on crystalline support. The density functional theory (DFT) demonstrated the strong metal-support interaction (SMSI) and adsorption energy varying with different sizes of Pt/supports. Especially, the synergy between the single-atom structure and the amorphous Fe₂O₃ successfully weakens CO poisoning and promotes the activation of O₂ near the Pt and Fe₂O₃ surface, accelerating the CO oxidation kinetics. The study also revealed that the amorphous structure could be a practicable approach to enhance the catalytic performance of CO oxidation catalysts.

2. Results and Discussion

2.1. Structural Characterization of Amorphous Fe₂O₃-Supported Different Size Pt Catalysts

The Pt/Fe₂O₃ catalysts were prepared by a solvothermal method. The ethylene glycol (EG) is important for the formation of amorphous Fe₂O₃ nanosheets.^[20] Unlike the layered materials, iron oxide phases, usually do not possess layered crystalline structures, henceforth, EG is needed to facilitate the formation of an amorphous Fe₂O₃ nanosheet rather than a nanoparticle form.^[21] The effect of EG on facilitating the formation of iron oxide nanosheets may be related to the complexation of EG with iron species during the dissociation and condensation reactions, as well as the suppress crystal growth along the

other surfaces.^[20,22] By varying the amount of Pt loading and solvent, the dispersion and size of Pt metal were well controlled with their morphologies varying from isolated single atoms, loosely associated atoms clusters, sub-nanoparticles to 3D large nanoparticles. **Figure 1a,c,e** presents the representative transmission electron microscopy (TEM) images of the as-prepared Pt-SA/A-Fe₂O₃, Pt-SC/A-Fe₂O₃, and Pt-SN/A-Fe₂O₃, respectively. The Pt-SA/A-Fe₂O₃ samples displayed a clean-surface nanosheets structure (Figure 1a), while the Pt-SC/A-Fe₂O₃ displayed dust-like points on surface (Figure 1c) and Pt-SN/A-Fe₂O₃ has small particles (1–2 nm) on the nanosheets substrates (Figure 1e). Moreover, the average thickness of the different catalysts nanosheets was ≈3.1 nm, according to the high-angle annular dark-field scanning transmission electron microscopy (HAADF-STEM) and high-resolution TEM (HRTEM) measurements for the thickness of the nanosheets, which is ultrathin to efficiently expose the active sites in catalytic reactions (Figure S1, Supporting Information). Figure 1b and insert show the HAADF-STEM images of Pt-SA/A-Fe₂O₃, which can identify the heavy atoms.^[1a,13] As clearly revealed by bright spots contrasted with the dark substrate and marked by the red circles, isolated atoms were dispersed on the surface of Fe₂O₃ nanosheets (Figure 1b). All the Pt species existed almost only as isolated single atoms; neither sub-nanometer clusters nor big nanoparticles were observed (Figure 1b, more images from different regions can be found in Figure S2, Supporting Information). On the contrary, when the Pt loading was more than 4.56 wt%, clustering of single atoms occurred and tiny clusters composed of loose and random ensembles of tens of atoms with dimensions 0.8–1.6 nm were formed (Figure 1d). Furthermore, when the Pt loading increased to 8.62 wt%, uniform small ripe sub-nanometer particles (≈2 nm) with occasional clusters were formed (Figure 1e,f). These morphologies varying from single atoms, atoms clusters to sub-nanoparticles were further verified by X-ray photoelectron spectroscopy (XPS) and X-ray diffraction patterns (XRD) of Pt/Fe with different Pt mass loadings (**Figure 2**). Figure S3 in the Supporting Information and Figure 2b show the full XPS spectrum and Fe 2p region XPS spectrum with the detailed deconvoluted XPS peaks (Figure S4, Supporting Information) of the three samples. All the three XPS spectra exhibited two peaks at ≈711.3 and ≈724.7 eV, which can be assigned to the Fe 2p 3/2 and Fe 2p 1/2 binding energies, respectively, indicating the oxidation status of Fe₂O₃.^[18b,23] The appearance of the small satellite peak in the XPS spectrum at ≈719.0 eV can further confirm the existence of Fe₂O₃ in the as-synthesized catalysts.^[23b] The XRD patterns in Figure 2a show that for all the three samples, no crystalline Fe₂O₃ peaks could be observed, indicating the amorphous nature of the Fe₂O₃ supports. For the Pt-SA/A-Fe₂O₃, there is even none Pt diffraction peaks because of only single-atom structures and extremely low mass loading which could not be detected.^[1b] For the Pt-SC/A-Fe₂O₃, also very negligible signal of Pt can be found, in agreement with the form of tiny Pt clusters and aggregates composed by tens of Pt atoms. In Pt-SN/A-Fe₂O₃, the peaks of fcc Pt were clearly observed due to the existence of Pt ripe particles with ordered lattice, indicating the co-existence of Pt nanoparticles and the amorphous Fe₂O₃ in this catalyst.

We also carried out the HRTEM (Figure 2c–e), selected area electron diffraction (SAED, Figure 2f–h), and HAADF-STEM

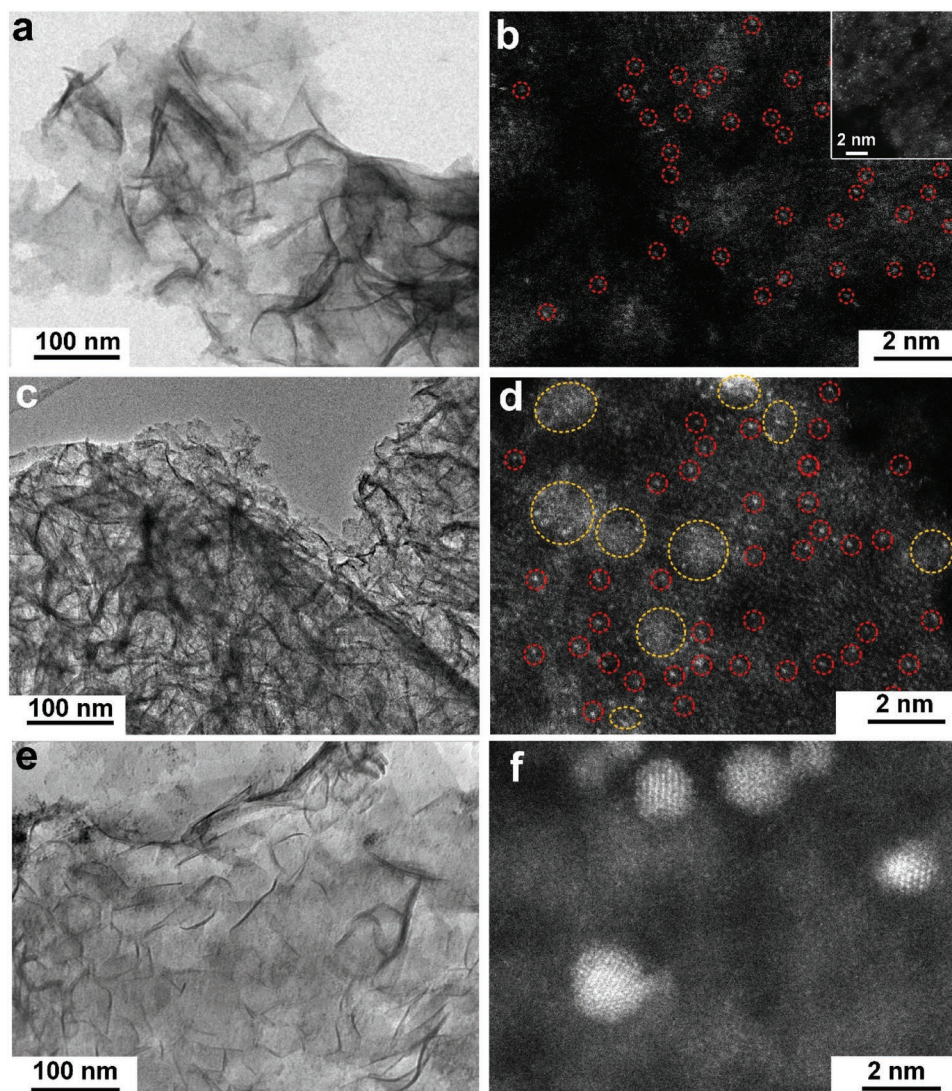


Figure 1. Structural characterizations of amorphous Fe_2O_3 sheets with different Pt contents. a) TEM image and b) HAADF-STEM image of Pt-SA/A- Fe_2O_3 . c) TEM image and d) HAADF-STEM image of Pt-SC/A- Fe_2O_3 . The red circles represent the atomically dispersed single-atom catalysts and the green circle is sub-nanoatom clusters. e) TEM image and f) HAADF-STEM image of Pt-SN/A- Fe_2O_3 .

(Figure 2i–k) images to investigate the detailed structure of the samples. As shown in Figure 2c–e, for all the three samples, there are no clear crystal lattice fringes in the Fe_2O_3 nanosheets. Furthermore, the SAED pattern images of the nanosheet supports also showed no strong diffraction rings or speckles ascribed to iron oxide. All these results also further proved the existence of amorphous- Fe_2O_3 supports. The magnified HAADF-STEM images in Figure 2i–k revealed the single atoms, clusters, and nanoparticles state of Pt on the amorphous Fe_2O_3 substrate, respectively.

2.2. X-Ray Absorption Fine Structure Characterization and the Local Structure Characterization

The extended X-ray fine structure (EXAFS) and X-ray absorption near-edge spectroscopy (XANES) were carried out in order

to further prove the Pt atom states and understand the specific local electronic structure of the single-atom and cluster Pt catalysts (Figure 3a,b and Figure S5, Supporting Information). The Pt L_3 -edge XANES profiles in Figure 3a indicate that Pt species in Pt-SA/A- Fe_2O_3 were in a higher oxidation state than those in Pt-SC/A- Fe_2O_3 and Pt metallic foil, which was implied by the higher energy for absorption edge and the stronger intensity for the white line.^[1a,b] As known to all, CO has strong adsorption on pure Pt metal catalysts, which blocks its catalytic sites, resulting in the poison effect. It has been reported the higher oxidation state of Pt species, the back-donating interaction between CO and Pt will be much less, and so the more-vacant d orbitals of the individual Pt atoms in catalyst play a vital role in the remarkable catalytic activity of the catalyst.^[17c] It is worth noting that both the Pt-SA and Pt-SC catalysts showed peaks between the PtO_2 and Pt foil references. We can see that the Pt single atom displayed the highest oxidation state than the

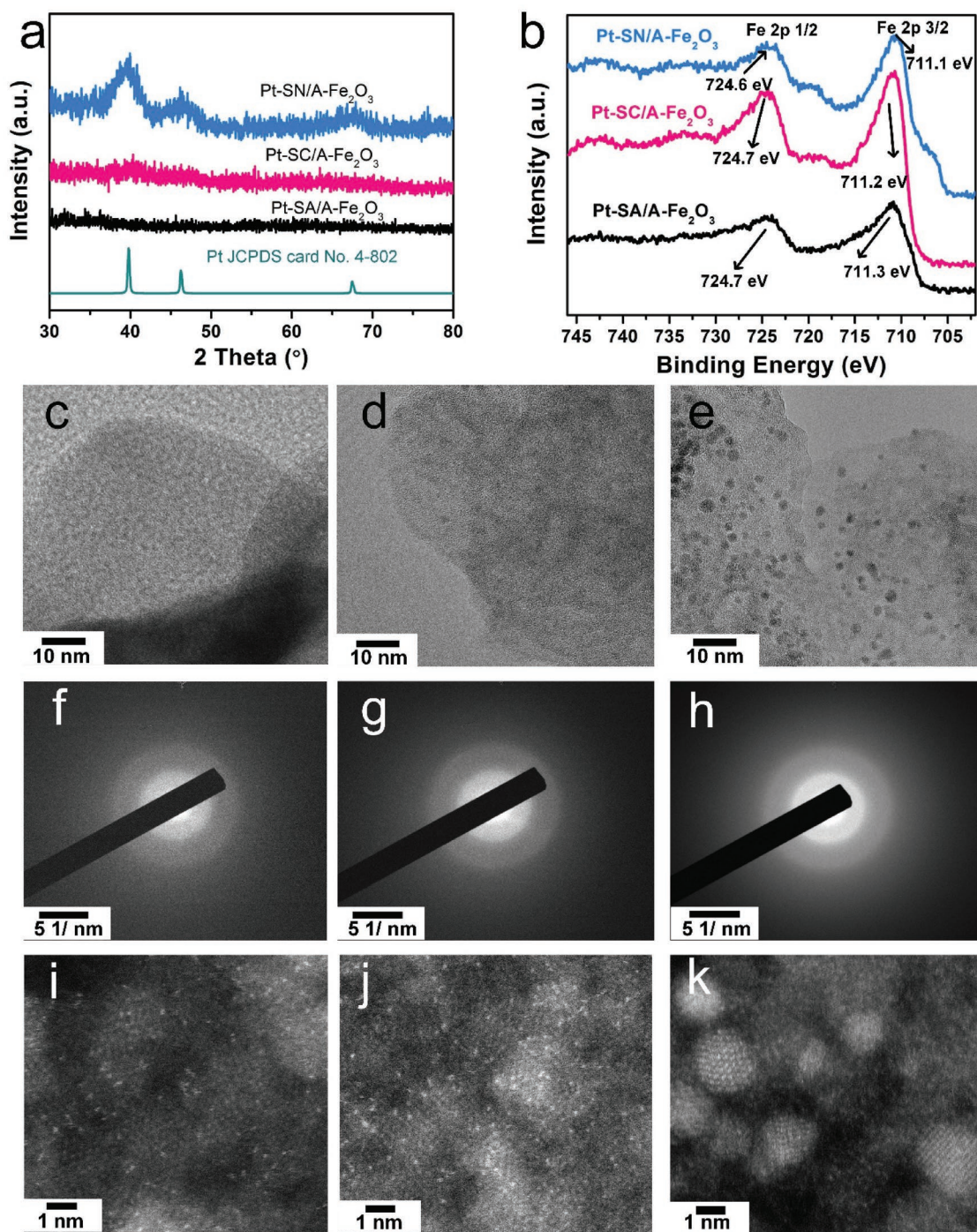


Figure 2. Nanoscale structural characterizations of the three different Pt catalysts on the amorphous Fe_2O_3 support. a) XRD and b) XPS of as-prepared Pt-SA/A- Fe_2O_3 , Pt-SC/A- Fe_2O_3 , and Pt-SN/A- Fe_2O_3 . c–e) HRTEM images, f–h) the SAED pattern, and i–k) the magnified HAADF-STEM image of c, f, i) Pt-SA/A- Fe_2O_3 , d, g, j) Pt-SC/A- Fe_2O_3 , and e, h, k) Pt-SN/A- Fe_2O_3 catalysts, respectively.

cluster structure and metallic nanoparticle, and henceforth this will weaken the interaction of CO and Pt, and also activate the C–O bond. Furthermore, as shown in EXAFS in R space (Figure 3b), Pt-SA/A- Fe_2O_3 exhibited a prominent peak at ≈ 1.7 Å from the Pt–O shell contribution. No other obvious typical peaks for Pt–Pt contribution were observed. Thus, Pt single atoms were finely dispersed throughout the entire amorphous Fe_2O_3

substrate. The fitting EXAFS curves are shown in Figure S6 in the Supporting Information, and the fitting EXAFS parameters and the coordination environment results for platinum are summarized in Table S2 in the Supporting Information. The fitted Pt–O coordination number for Pt-SA/A- Fe_2O_3 is ≈ 4.1 , indicating that each Pt atom coordinates with four oxygen atoms on the Fe_2O_3 support, what is more, it is reported this

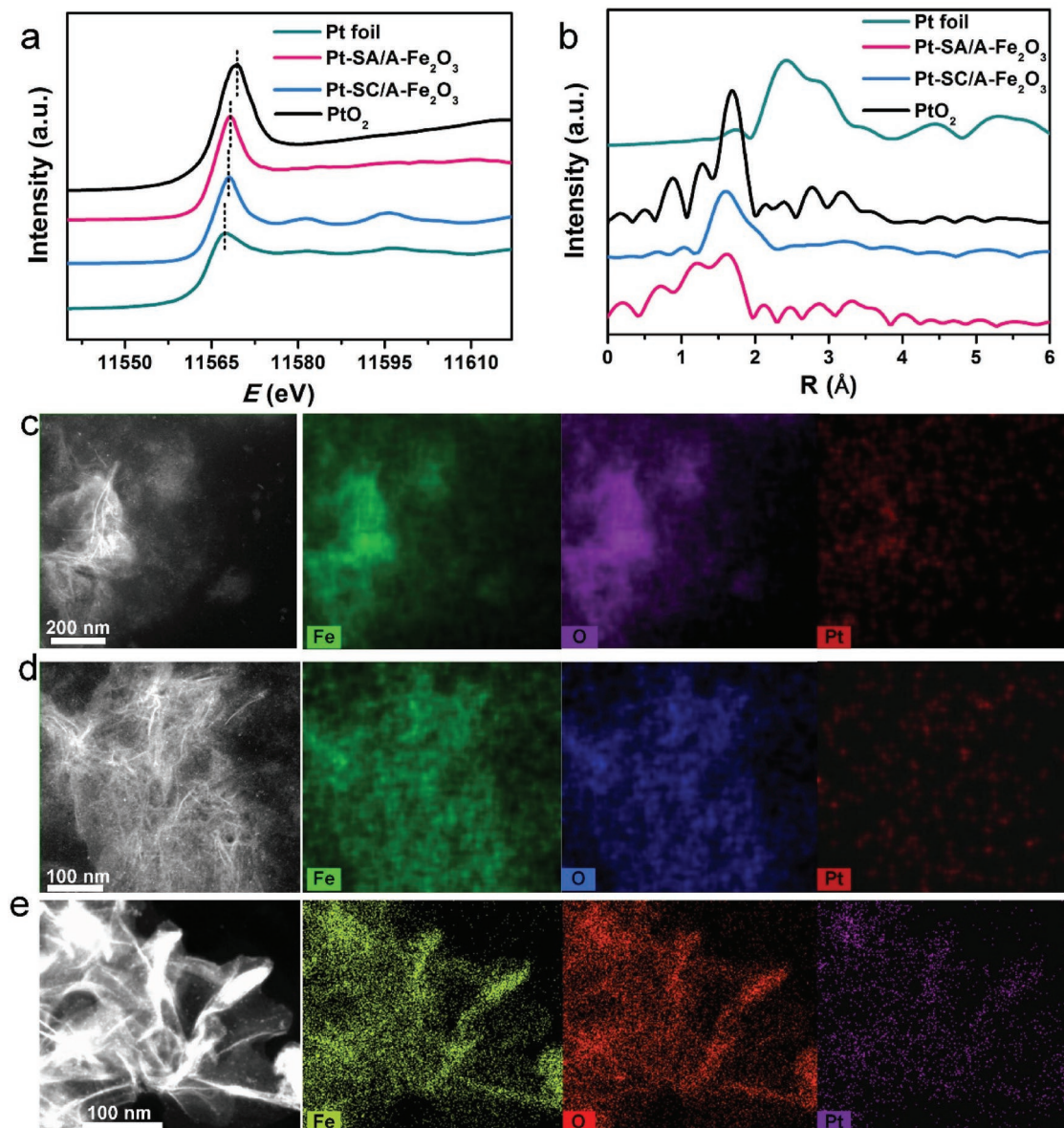


Figure 3. XAFS and EDX mapping study. Normalized a) XANES and b) EXAFS spectra of the Pt-SA/A-Fe₂O₃ and Pt-SC/A-Fe₂O₃, and the HAADF and corresponding STEM-EDS elemental mapping, of c) Pt-SA/A-Fe₂O₃, d) Pt-SC/A-Fe₂O₃, and e) Pt-SN/A-Fe₂O₃, respectively.

four-coordination structure is inherently preferred by zero or low valent Pt complexes, which may partially explain the good stability of the Pt single-atom catalyst in the catalysis, and the Pt–O bonding distance is close to that in PtO₂ suggests the strong metal–support interaction.^[1a,24] When the Pt loading was increased to 4.56 wt% (Pt-SC/A-Fe₂O₃), there was also a prominent peak in the range of ≈1.5–1.8 Å, and a very slight raised peak at ≈2.8 Å can be carefully observed, implying that the clusters with nearby Pt interactions started to appear (Figure 2j). However, their Pt–Pt coordination and shell were still relatively low compared with that of Pt foil, similar with that of Pt-SA/A-Fe₂O₃ catalyst, indicating the formation of very small (1.0 nm) Pt clusters composed by irregular Pt atoms. All of the above

XAFS results are consistent with the observation of the shape from the HAADF-STEM (Figure 2).

The inductively coupled plasma mass spectrometry (ICP-MS) was applied to investigate the loading of Pt, showing results of as high as 1.2 wt % for Pt-SA/A-Fe₂O₃, 4.56 wt% of Pt in Pt-SC/A-Fe₂O₃, and 8.62 wt% for Pt-SN/A-Fe₂O₃ (Table S1, Supporting Information), in consistent with the result trend obtained by the HAADF-STEM. Energy-dispersive X-ray spectroscopy (EDS) mapping analysis in an HAADF-STEM revealed the evenly dispersed Pt and Fe in the Pt-SA and Pt-SC/A-Fe₂O₃ (Figure 3c,d). Correspondingly, the STEM-EDS of Pt-SN/A-Fe₂O₃ further proved the form of sub-nano Pt particles on the nanosheets (Figure 3e).

2.3. Phase-Transformation of the Amorphous Substrate to Crystalline Supports

It should be noted that the single atoms of Pt were stabilized at a high concentration of 1.2 wt% in our synthetic process, probably due to the SMSI of the amorphous Fe₂O₃ nanosheets. Therefore, this 2D Fe structure is benefit for oxidation reaction.^[25] According to the above results from both HAADF-STEM and XANES/EXAFS, we have prepared three kinds of Pt structures anchored onto the amorphous Fe₂O₃ nanosheets, and in order to make a detailed comparison of the CO oxidation behavior between the amorphous and crystalline Fe₂O₃ supported catalyst, at the same time we also transformed the amorphous Fe₂O₃ support to crystallized ones and got the other three kind of catalysts via annealing at 300 °C, named Pt-SA/C-Fe₂O₃, Pt-SC/C-Fe₂O₃, and Pt-SN/C-Fe₂O₃. As can be seen from **Figure 4a**, after annealing process, all the XRD patterns of the three Pt/Fe₂O₃ catalysts displayed obviously Fe₂O₃ diffraction peaks, indicating the formation of Fe₂O₃ crystallized structure, in good agreement with the typical HRTEM (**Figure 4b,d,f**) and the corresponding magnified HAADF-STEM images in **Figure 4c,e,g**, which exhibited clearly crystal lattice fringes in the 2D sheets structures of Fe₂O₃. In detail, as depicted in the HAADF-STEM images (**Figure 4c,e,g**) corresponding to the Pt single atom, cluster, and nanoparticle on Fe₂O₃ after annealing, it is worth noting that the Pt state on the fine latticed supports by annealing treatment was not obviously impacted and nearly the same as their atomic structures in the amorphous Fe₂O₃. Henceforth, combining the above three Pt/A-Fe₂O₃ and the three Pt/C-Fe₂O₃ catalysts, we have good model catalysts to study the structure–function relations for the different-sized platinum catalysts and the amorphous/crystalline supports effects toward CO oxidation reaction.

2.4. CO Oxidation on Different Catalysts

CO oxidation experiments were carried out at a fixed flow mixture of CO, O₂, and N₂ at a constant hourly space velocity (constant weight of catalyst). CO oxidation on Pt-SA/A-Fe₂O₃, Pt-SC/A-Fe₂O₃, and Pt-SN/A-Fe₂O₃ initiates at approximately 10, 20, and 50 °C, respectively (**Figure 5**). Correspondingly, the initiating temperature for the Pt-SA/C-Fe₂O₃, Pt-SC/C-Fe₂O₃, and Pt-SN/C-Fe₂O₃ was approximately 30, 30, and 50 °C. The results clearly show that Fe₂O₃-supported single Pt atoms or atomic clusters are catalytically active for the oxidation of CO at room temperature. In addition, the CO oxidation is easier in low temperature for the amorphous Fe₂O₃-supported Pt catalysts than their crystalline ones. For example, at 30 °C, the Pt-SA/A-Fe₂O₃ converted CO by ≈20% while the crystalline counterpart (Pt-SA/C-Fe₂O₃) converted CO only 8%. Furthermore, the CO conversion of the different samples differed from each other significantly. As shown in **Figure 5**, the CO conversion is achieved to 100% at near 70 °C for the Pt-SA/A-Fe₂O₃ catalyst, and those T₁₀₀ (the lowest temperatures to reach 100% efficiency of CO conversion) for Pt-SC/A-Fe₂O₃, Pt-SN/A-Fe₂O₃ are ≈80 and ≈110 °C, respectively. However, for the Pt-SA/C-Fe₂O₃, Pt-SC/C-Fe₂O₃, and Pt-SN/C-Fe₂O₃ catalysts, the T₁₀₀ are ≈80, ≈100, and 125 °C, which were higher

than their amorphous forms by ≈10, ≈20, and 15 °C, respectively. These results also confirm the more active performance of single-atom catalyst, as well as indicating the amorphous Fe₂O₃ support is beneficial for the CO oxidation. To further investigate the active performance, the specific rate at 60 °C was measured according to the average activity at 20, 40, and 60 min. Additionally, the corresponding turnover frequency (TOF) of the catalysts was also calculated to obtain the intrinsic activity for further comparison of their size effects and supports influence. As shown in **Table 1**, the Pt-SA/A-Fe₂O₃ gave a specific reaction rate of 1.25 mol_{CO} h⁻¹ g_{Pt}⁻¹ at the reaction temperature of 70 °C, which is 7.1 times that of Pt-SC/A-Fe₂O₃ catalyst and almost 26.4 times than that of Pt-SN/A-Fe₂O₃. As expected, it implied a slower specific rate for the crystalline Fe₂O₃-supported Pt (**Table 1**), which shows that the Pt-SA/A-Fe₂O₃ is 1.53 time of the Pt-SA/C-Fe₂O₃ toward the specific rate. What is more, the other two kinds of Pt on crystalline Fe₂O₃ exhibited poorer specific rate than the amorphous forms. The TOFs also showed that Pt-SA/A-Fe₂O₃ was 7 times and 26.4 times more active than Pt-SC/A-Fe₂O₃ and Pt-SN/A-Fe₂O₃. Further study on TOFs for the crystalline Fe₂O₃-supported Pt also indicated the superior performance of amorphous materials (**Table 1**). All these results indicated that our Pt-SA catalyst was the most active for CO oxidation among the different-sized Pt catalysts from single atom to nanoparticles and the amorphous Fe₂O₃ structure is beneficial for the rapid CO oxidation. It can be found that our work exhibited comparable performance toward the other reports on superior CO oxidation catalysts to date (**Table S3**, Supporting Information). The high activity of single-atom catalyst on the amorphous supports must have originated from the intrinsic nature of single Pt atoms dispersed onto Fe₂O₃ surfaces. We further investigated the long-term-use stability of the Pt-SA/A-Fe₂O₃ catalyst. The morphology and the structure state of the atomically dispersed Pt-SA/A-Fe₂O₃ catalyst using HAADF-STEM, HRTEM, and SAED after the CO oxidation test (**Figure S7**, Supporting Information). As a result, the single-atomic dispersion of Pt was still well maintained without aggregation. Moreover, the HRTEM did not show any crystalline lattices after the CO oxidation and the further SAED image still displays no obvious diffraction rings or speckles as its original state before CO oxidation, suggesting the retained amorphous structure of the Fe₂O₃ in Pt-SA/A-Fe₂O₃. In addition, the CO oxidation performance of the Pt-SA/A-Fe₂O₃ catalyst after the stability test showed that the CO conversion at different temperatures was similar before and after the 30 h stability test (**Figures S8 and S9**, Supporting Information). Specifically, the CO conversion at 70 °C was 93.8% after 30 h, giving a specific reaction rate of 1.17 mol_{CO} h⁻¹ g_{Pt}⁻¹, indicating no obvious degradation compared to the performance at 0 h (97.2%, 1.25 mol_{CO} h⁻¹ g_{Pt}⁻¹). All these results suggested the good stability of the Pt-SA/A-Fe₂O₃ catalyst.

2.5. Understanding of Relation between Catalytic Activity and Catalysts Surface Properties

To elucidate the nature of the exceptionally high catalytic activity of Pt single-atom catalyst on the amorphous Fe₂O₃, relativistic DFT calculations were carried out to give extensive

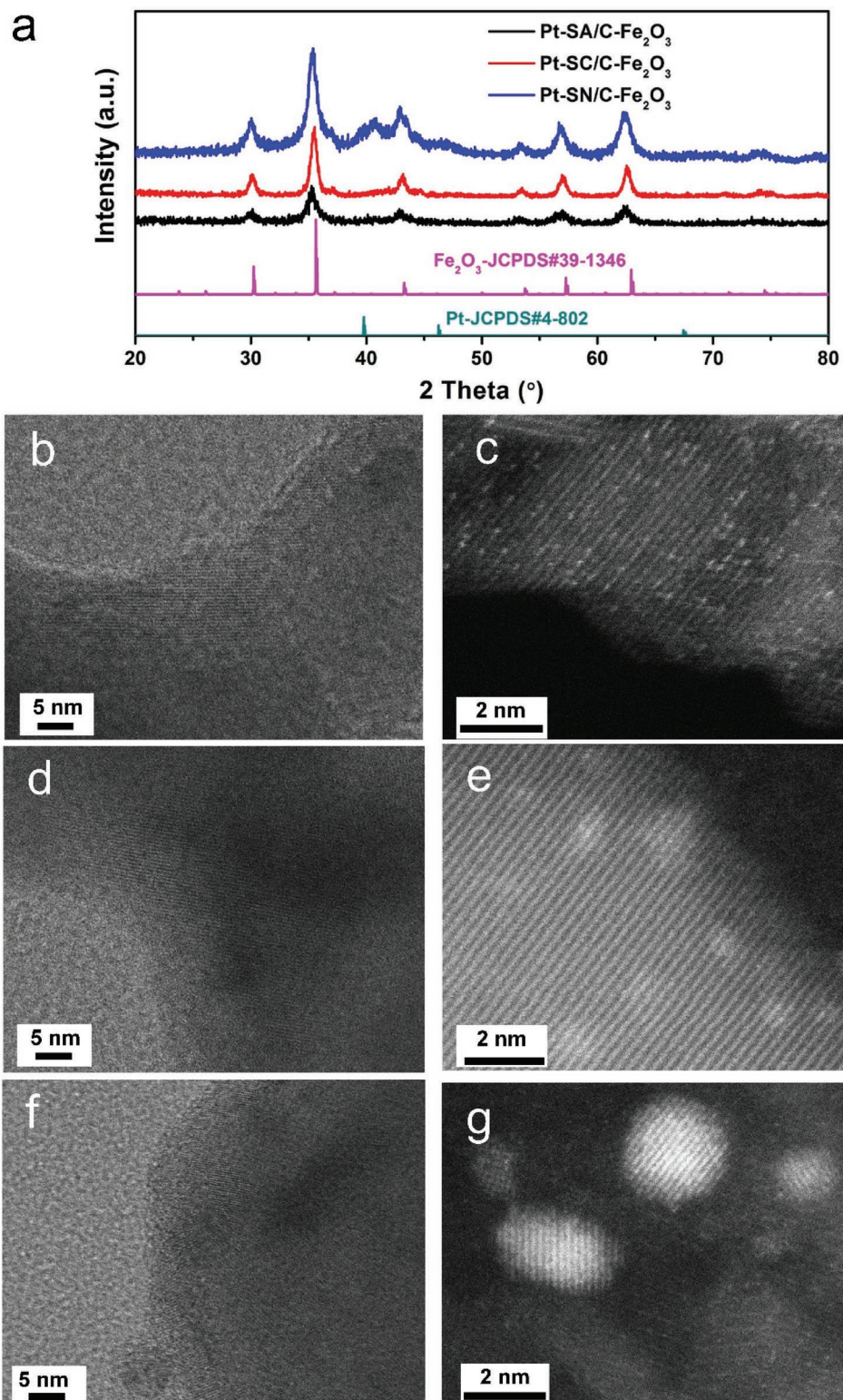


Figure 4. Structural characterizations of the three different Pt catalysts on the crystallized Fe₂O₃ support. a) XRD pattern, b,d,f) the HRTEM, and c,e,g) the corresponding HAADF-STEM images of the b,c) Pt-SA/C-Fe₂O₃, d,e) Pt-SC/C-Fe₂O₃, and f,g) Pt-SN/C-Fe₂O₃, respectively.

theoretical investigations. To explore the interfacial interaction of the Pt species with the Fe₂O₃, we studied the charge interaction between them by using the Bader charge analysis method

(Figure 6a–c). As expected, electron transfer occurs from different Pt species to the Fe₂O₃ surfaces, leading to a positive charge on Pt. This electron transfer leads to the stronger

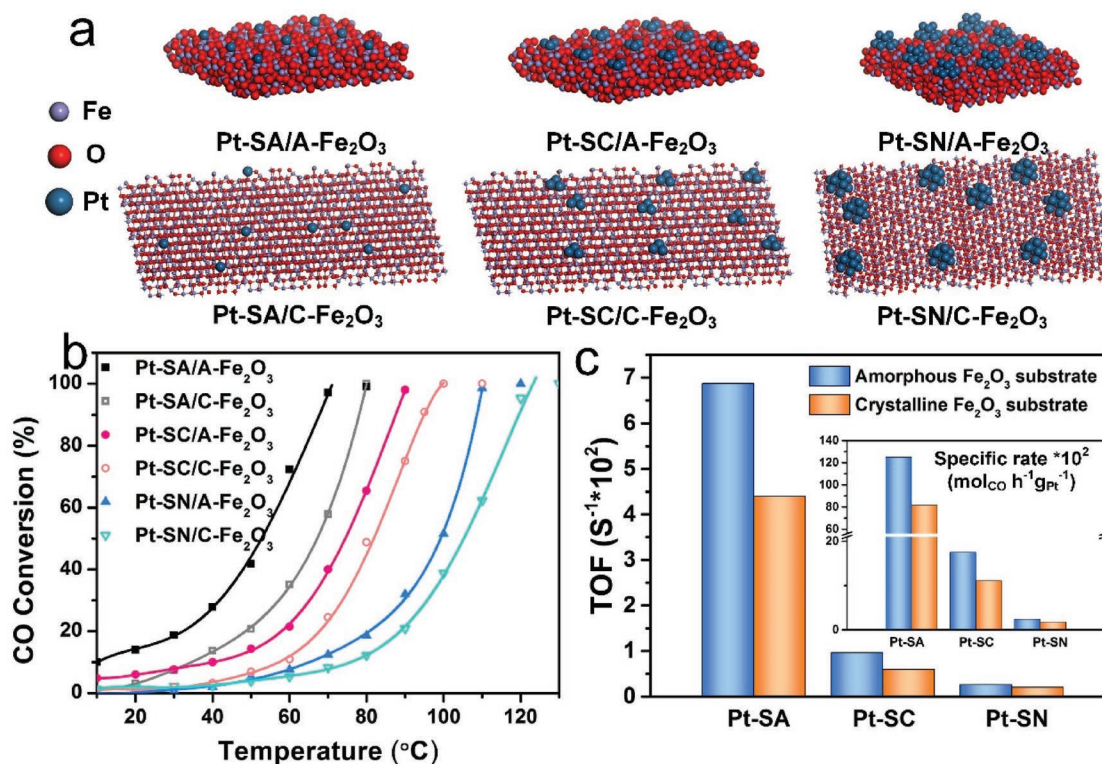


Figure 5. CO oxidation performance of the three different Pt catalysts on the two Fe₂O₃ supports. a) Schematic of the different Pt/Fe₂O₃ structures, different sizes were used to distinguish the elements, b) CO conversion, the different color curves represent the fitting curves for the CO performances based on the temperatures of different catalysts, respectively, c) TOFs and specific rates (inset).

interfacial interactions, which has been reported as an important influence on surface reactivity.^[1a,26,27] The Bader charge analysis revealed that the amount of charge transfer (Δq) is 0.746, 0.221, and 0.114 eV per atom for Pt SA, SC, and SN on the amorphous Fe₂O₃ surfaces (Table S4, Supporting Information), respectively, indicating that the strongest interfacial interaction between Pt-SA and Fe₂O₃ than the other catalysts, which was in consistence with the CO oxidation performance. The binding energy of Pt species with Fe₂O₃ (Figure 6d and Table S5, Supporting Information) also proved the strongest interaction of Pt SA with the Fe₂O₃. To further reveal the nature of the high reactivity on Pt-SA/A-Fe₂O₃, we calculated the adsorption energy for CO and O₂ (Figure 6e and Table S6, Supporting Information). The adsorption energy of CO appears a

tendency of increasing while the stable adsorption energy of O₂ decreases remarkably in the order of Pt-SA/A-Fe₂O₃, Pt-SC/A-Fe₂O₃ to Pt-SN/A-Fe₂O₃. This is a clear demonstration that the CO poisoning effect of Pt-SA/A-Fe₂O₃ is the weakest and the activation of O₂ for Pt-SA/A-Fe₂O₃ is the strongest, both leading to a highest CO oxidation performance of the Pt-SA/A-Fe₂O₃ catalyst. To further prove the CO adsorption performance, the electrochemical CO stripping experiments were carried out for the above three samples, which can be seen in Figure S10 in the Supporting Information. It definitely showed the peak density of CO oxidation in the sequence Pt-SA/A-Fe₂O₃ < Pt-SC/A-Fe₂O₃ < Pt-SN/A-Fe₂O₃. Furthermore, the peak potential positions were 0.713, 0.718, and 0.738 V for these three samples, respectively, indicating the weakest CO adsorption on Pt single atoms. For the Pt-SC and Pt-SN catalysts, their CO adsorption was stronger and the O₂ interaction was much reduced, both of which lead to a suppressed CO oxidation. The d-band center of Fe shows down-shift trends for Pt-SA/A-Fe₂O₃, Pt-SC/A-Fe₂O₃ to Pt-SN/A-Fe₂O₃ (Figure 6f,g and Figures S11 and S12 and Table S7, Supporting Information), indicating the decreased O₂ interaction, agreeing with the calculated adsorption energy. Moreover, to further understand the effect from the oxygen vacancy structure conditions in the two kinds of supports, electron paramagnetic

Table 1. Comparison of specific rates and TOFs of different Pt/Fe₂O₃ catalysts at 70 °C.

| Samples | Pt loading [wt%] | d_{Pt} [nm] | Specific rate $\times 10^2$ [mol _{CO} h ⁻¹ g _{Pt} ⁻¹] | TOF $\times 10^2$ [s ⁻¹] |
|--|------------------|---------------|--|--------------------------------------|
| Pt-SA/A-Fe ₂ O ₃ | 1.2 | - | 125.0 | 6.87 |
| Pt-SC/A-Fe ₂ O ₃ | 4.56 | ≈1.2 | 17.5 | 0.96 |
| Pt-SN/A-Fe ₂ O ₃ | 8.62 | ≈2 | 2.37 | 0.26 |
| Pt-SA/C-Fe ₂ O ₃ | 1.2 | - | 81.6 | 4.4 |
| Pt-SC/C-Fe ₂ O ₃ | 4.56 | ≈1.2 | 11.07 | 0.60 |
| Pt-SN/C-Fe ₂ O ₃ | 8.62 | ≈2 | 1.78 | 0.20 |

Note: TOF was calculated based on Pt dispersion (mol CO_{ox}/mol surface Pt). All the single-atom Pt atoms were used for calculation for Pt-SA/A-Fe₂O₃ and Pt-SA/C-Fe₂O₃. Pt dispersion of Pt-SC/A-Fe₂O₃, Pt-SN/A-Fe₂O₃, Pt-SC/C-Fe₂O₃, and Pt-SN/C-Fe₂O₃ were estimated by the Pt size according to $D = 1/d_{Pt}$.

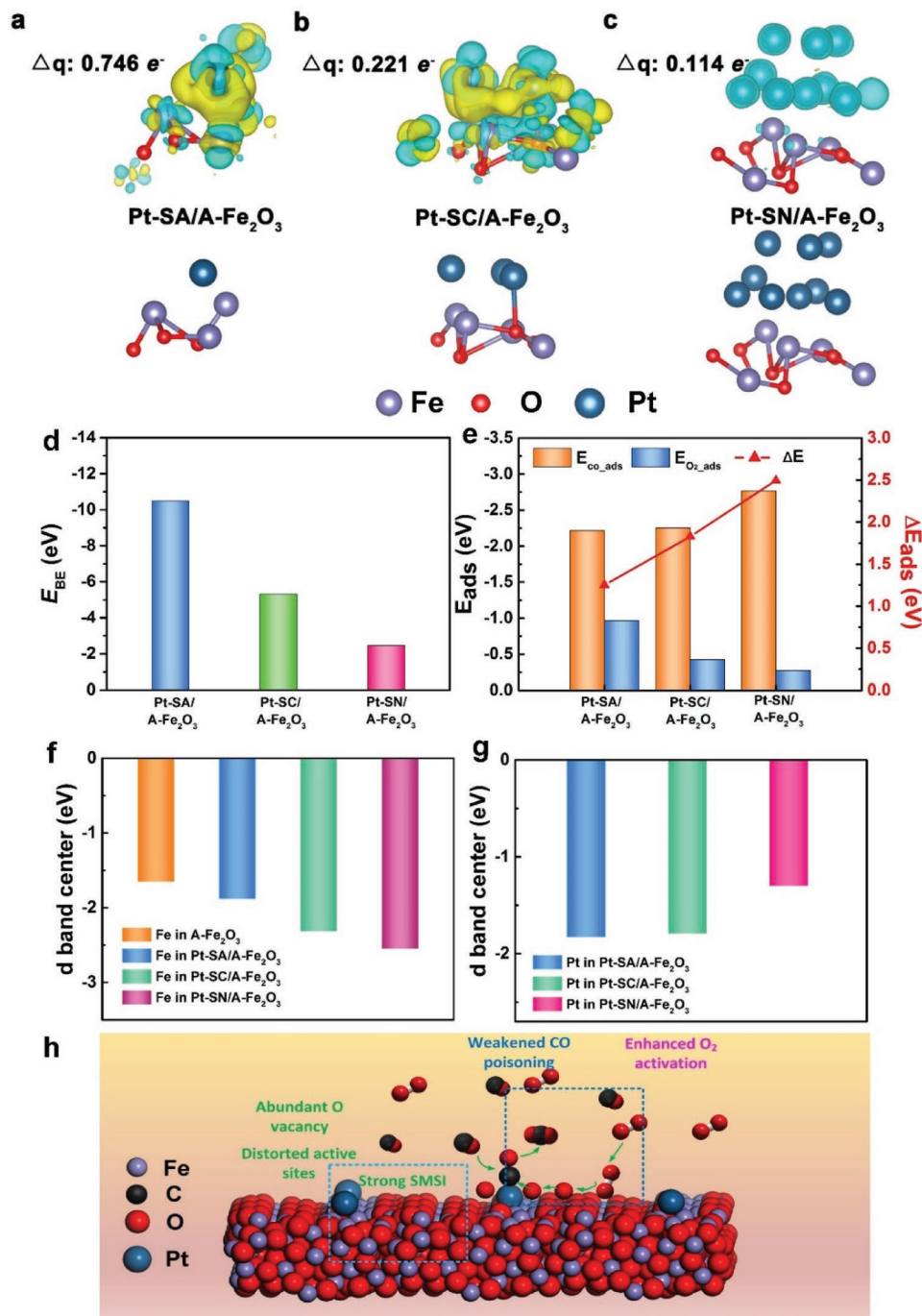


Figure 6. DFT calculation of the electrons transfer and adsorption energy. Charge density difference and the separate atomic model of a) Pt-SA/A-Fe₂O₃, b) Pt-SC/A-Fe₂O₃, and c) Pt-SN/A-Fe₂O₃, respectively. Yellow regions represent electron depletion and blue ones denote electron accumulation with an isosurface value of 0.1 electrons Å⁻³. Numerical values are given in units of e based on Bader charge analysis. d) The binding energy between Pt-SA/A-Fe₂O₃, Pt-SC/A-Fe₂O₃, and Pt-SN/A-Fe₂O₃. e) The stable adsorption energy of CO and O₂ for Pt-SA/A-Fe₂O₃, Pt-SC/A-Fe₂O₃, Pt-SN/A-Fe₂O₃; and the energy difference ΔE between E_{ads-CO} and E_{O_2-ads} , f) the comparison among the d-band center of Fe in A-Fe₂O₃ and the three different catalysts, g) the comparison of d-band center of Pt in the three different catalysts, and h) mechanism and process of CO oxidation on Pt-SA/A-Fe₂O₃.

resonance was used to detect the unpaired electrons in the Pt-SA/A-Fe₂O₃ and Pt-SA/C-Fe₂O₃ samples (Figure S13, Supporting Information). It can be seen that Pt-SA/A-Fe₂O₃ exhibited a signal at g value of 2.003 (Figure S13, Supporting Information), which could be identified as the electrons

trapped on O-vacancies, suggesting that abundant oxygen vacancies emerged on the surface of Pt-SA/A-Fe₂O₃. It has been widely reported that the O₂ activation was more efficient in the amorphous surface with more vacancies and distorted active sites than the crystalline supported one,^[28] which well

explained the superior performance of Pt-SA/A-Fe₂O₃ than that of Pt-SA/C-Fe₂O₃.

Based on our study, it is believed that the CO oxidation for the Pt/Fe₂O₃ was catalyzed in a Langmuir–Hinshelwood pathway, and the reaction mechanism for the Pt-SA/A-Fe₂O₃ can be described as Figure 6h. It has been reported that the CO oxidation reaction of Pt catalysts over non-supports occurs very slowly at low temperature because oxygen adsorption can easily be blocked by a saturated layer of adsorbed CO on the Pt surface.^[29] However, when supported on iron oxides substrate materials, the Pt metal will play the role in adsorbing and active CO molecule, while the Fe₂O₃ substrates will be considered to activate the O₂ from the gas environment in relatively low temperature. Subsequently, the activated CO will react with the active O species to form CO₂ and finish the CO oxidation process.^[30] In our work, the amorphous Fe₂O₃ played two critical roles which were beneficial for the CO oxidation. On the one hand, the Fe₂O₃ interacted with the Pt species will induce strong metal–support interactions, which could change the state of Pt. As can be seen from the XANES results (Figure 3a), the Pt in Pt-SA/A-Fe₂O₃ existed with high oxidation state, indicating the presence of high-valence Pt atoms, which could help to reduce the CO adsorption energy for CO oxidation,^[2] which is also indicated by DFT in Figure 6. On the other hand, the amorphous Fe₂O₃ substrate with abundant oxygen vacancies was beneficial for the activation of the O₂ near the catalysts surface from the supplying hybrid gas. The abundant and easier-produced active O species will react with the CO adsorbed near the Pt to form CO₂, which as a result, accelerated the CO oxidation process.^[28b,c,31] In addition, the distorted structure would likely provide more such active sites for reaction,^[19b,28a,32] which exhibit isotropic molecular diffusion and supply more percolation pathways to accelerate the fast diffusion of gas species in the process.^[18b]

3. Conclusion

In summary, we reported a series of Pt catalysts on amorphous structure Fe₂O₃ ultra nanosheets from single-atom, clusters to sub-nanoparticles with the different loading contents of Pt. The atomically dispersed Pt single atoms on ultrathin amorphous Fe₂O₃ nanosheets show great promise for catalysis due to the high specific surface area, full exposed atoms sites, and the synergistic effect between the atomically dispersed Pt single atoms and the amorphous Fe₂O₃ supports which could easily activate the CO oxidation, as well as its open framework and fast diffusion for the reacting gas species.^[18b,23a,28c,33] Furthermore, we compared the CO oxidation performance among the size effect as well as the support effect between amorphous and crystalline forms. Specifically, the Pt-SA/A-Fe₂O₃ catalyst showed extremely superior activity for CO oxidation reactions because: 1) the strong binding and stabilization of single Pt atoms coming from the SMSI between the in situ locally synthesized Pt atoms and Fe₂O₃ supports; 2) the single-atom configuration leads to a weak CO adsorption on Pt and an enhanced O₂ adsorption on nearby Fe₂O₃; 3) the very close neighbored amorphous Fe₂O₃ species substrate possessed many defects and O-vacancies is easy to interact with oxygen and provides active abundant sites to acti-

vate huge amount of O due to its specific characteristic, which could further facilitate the CO_{ad} oxidation on the neighboring Pt or the interface between Pt and Fe₂O₃. All of these synergistic effects ultimately account for the excellent catalytic activity. Our study provides a promising facile approach for the synthesis of highly active and stable single-atom catalysts with amorphous supports based on single Pt atoms and clusters, which have a great potential to reduce the high cost of industrial, commercial noble-metal catalysts in many applications or industry.

4. Experimental Section

Chemicals and Materials: Platinum(II) acetylacetonate (Pt(acac)₂, Strem Chemical, 98%), Iron(III) acetylacetonate (Fe(acac)₃, Strem Chemical, 98%), tungsten hexacarbonyl (W(CO)₆, Strem Chemical, 99%), EG (Sinopharm Chemical Reagent Co., Ltd., AR), N,N-dimethylformamide (DMF, Sinopharm Chemical Reagent Co., Ltd., AR) were purchased. Carbon monoxide (CO, 5%), oxygen (O₂, 5%), nitrogen (N₂, 99.999%), and argon (Ar, 99.999%) were purchased from Shanghai Weichuang Standard Gas Analytical Technology Co., Ltd.

Synthesis of Pt Single Atoms on Amorphous Fe₂O₃ Nanosheets: In a typical synthesis, Pt(acac)₂ (0.025 mmol), Fe(acac)₃ (3.14 mmol), and 150 mg W(CO)₆ were mixed into 15 mL of EG under room temperature under stirring. After the precursors were dissolved, the mixed solution was transferred to the Teflon-lined stainless-steel autoclaves and heated at 120 °C for 42 h. The final product was washed and collected with ethanol, deionized water, and acetone for two times, by centrifugation at 8000 rpm for 5 min, respectively. The above product was then transferred to a 60 °C oven in air condition for 6 h, and this product was used as the catalysts for the CO oxidation.

Synthesis of Pt Single Atoms with Clusters on Amorphous Fe₂O₃ Nanosheets and Pt Sub-Nanoparticles on Amorphous Fe₂O₃ Nanosheets: The method was similar as the single-atom catalyst, except the usage of Pt(acac)₂ is 0.075 and 0.12 mmol, respectively.

Transformation of Amorphous Substrate to Crystalline Fe₂O₃ Phase: The above-obtained Pt/A-Fe₂O₃ materials were then annealed in a glass tube furnace at 300 °C for 30 min in Ar condition and then collected the products for characterization.

Characterization: The loadings of Pt were measured on ICP spectrometer on a 6300 instrument (Thermo Electron Corp.). XRD patterns were recorded by using a SmartLab with Cu K α radiation ($\lambda = 1.54178 \text{ \AA}$). The TEM was carried out on a JEM-2800, and a JEM-2100F field emission electron microscope at an acceleration voltage of 200 kV. The HRTEM, HAADF-STEM, and the corresponding EDS mapping analyses were performed on a JEOL JEM-ARM200F S/TEM with a spherical aberration corrector and Grand ARM S/TEM at 300 kV with both image and probe corrector.

The X-Ray Absorption Fine Structure Measurements (XAFS): XAFS data of the samples over Pt L₃-edge were collected in transmission mode at the Advanced Photon Source located within the Argonne National Laboratory (Beamline 20 BM). Pt foil and PtO₂ were used as reference samples and measured in the transmission mode. XAS data were processed and analyzed using Athena and Artemis. For the XANES part, the experimental absorption coefficients as function of energies $m(E)$ were processed by background subtraction and normalization procedures, which were reported as “normalized absorption.”

CO Oxidation Catalytic Tests: The catalytic performances of samples for CO oxidation were evaluated in a fixed-bed reactor. The powder samples were packed between quartz wool with a thermocouple placed touching the sample inside the reactor. Prior to the tests, the samples were pelletized and sieved to 60 mesh for use. Approximately 60 mg of the samples and diluted with about 1 g of SiO₂ powder were loaded into a straight-shaped quartz reactor. The feed gas containing 1 vol% CO, 1 vol% O₂, and balance N₂ was allowed to pass through the reactor at a flow rate of 18.75 mL min⁻¹ (corresponding to a

space velocity of 18 750 mL h⁻¹ g_{cat}⁻¹). The effluent gas compositions were analyzed on-line by a gas chromatograph (GC-2014, Shimadzu). The CO conversions were calculated based on the difference between inlet and outlet concentrations. The CO oxidation long-term stability for the highest performance Pt-SA/A-Fe₂O₃ catalyst was as follows. The Pt-SA/A-Fe₂O₃ catalyst was treated to continuously catalyze the CO oxidation under the same CO oxidation operating conditions in 80 °C (in the temperature of the complete 100% CO conversion), and in the same presence of other environmental conditions (such as 1 vol% CO, 1 vol% O₂, and balance N₂). After 30 h treatment, the CO oxidation performance was explored again to compare with its initial state.

TOF Measurements and Calculation: The specific reaction rates and TOFs of the catalyst were obtained at specific temperatures CO conversion used to calculate the TOF and reaction rate was the average of three results at 20, 40, and 60 min. The dispersion of single-atom catalyst was 100% and those of other Pt/Fe₂O₃ were calculated according to $D = 0.9/d_{Pt}$, where d means the average diameter of supported Pt clusters.

DFT Calculation Methods: A detailed description of computational models and methods was provided. The DFT calculations were performed using the Vienna Ab initio Simulation Package^[34] code with the PW91 generalized gradient approximation,^[35] projector-augmented wave^[36] pseudopotentials, and a cut-off energy of 520 eV for the plane-wave expansion of the wave functions. Ground-state atomic geometries were obtained by minimizing the total free energy change and the band structure energy change between two steps both smaller than 1×10^{-4} eV. To model Pt-SA/A-Fe₂O₃, Pt-SC/A-Fe₂O₃, and Pt-SN/A-Fe₂O₃, single Pt atom, Pt cluster consisting of three atoms, and Pt nanoparticle consisting of ten atoms with half of Wulff structure were chosen, on the amorphous Fe₂O₃ model, respectively. A Monkhorst–Pack grid of size $1 \times 1 \times 1$ was used to sample the surface Brillouin zone,^[37] and the repeated slabs were separated from their neighboring images by a 15 Å width vacuum in the direction perpendicular to the surface.

Supporting Information

Supporting Information is available from the Wiley Online Library or from the author.

Acknowledgements

The work was sponsored by the thousand talents program for distinguished young scholars from Chinese government, National Key R&D Program of China (no. 2017YFB0406000), and the National Science Foundation of China (51521004, 51420105009, 51602196, and 21875137), and start-up fund (J.W.), the Zhi-Yuan Endowed fund (T.D.), and the support from Center of Hydrogen Science and Joint research center for clean energy materials from Shanghai Jiao Tong University. W.G. was supported by National Science Foundation with the grant number CBET-1159240 (X.P.) and the School of Engineering at University of California, Irvine. H.Z. thanks the computing resources from Shanghai Jiao Tong University Supercomputer Center.

Conflict of Interest

The authors declare no conflict of interest.

Keywords

amorphous, CO oxidation, Fe₂O₃, Pt, single atom

Received: May 28, 2019

Revised: July 13, 2019

Published online: August 15, 2019

- [1] a) B. T. Qiao, A. Q. Wang, X. F. Yang, L. F. Allard, Z. Jiang, Y. T. Cui, J. Y. Liu, J. Li, T. Zhang, *Nat. Chem.* **2011**, *3*, 634; b) H. S. Wei, X. Y. Liu, A. Q. Wang, L. L. Zhang, B. T. Qiao, X. F. Yang, Y. Q. Huang, S. Miao, J. Y. Liu, T. Zhang, *Nat. Commun.* **2014**, *5*, 5634; c) H. Yan, Y. Lin, H. Wu, W. H. Zhang, Z. H. Sun, H. Cheng, W. Liu, C. L. Wang, J. J. Li, X. H. Huang, T. Yao, J. L. Yang, S. Q. Wei, J. L. Lu, *Nat. Commun.* **2017**, *8*, 1070; d) J. Jones, H. F. Xiong, A. T. Delariva, E. J. Peterson, H. Pham, S. R. Challa, G. S. Qi, S. Oh, M. H. Wiebenga, X. I. P. Hernandez, Y. Wang, A. K. Datye, *Science* **2016**, *353*, 150; e) B. T. Qiao, A. Q. Wang, L. Li, Q. Q. Lin, H. S. Wei, J. Y. Liu, T. Zhang, *ACS Catal.* **2014**, *4*, 2113.
- [2] X. F. Yang, A. Q. Wang, B. T. Qiao, J. Li, J. Y. Liu, T. Zhang, *Acc. Chem. Res.* **2013**, *46*, 1740.
- [3] Z. Y. Li, Z. Yuan, X. N. Li, Y. X. Zhao, S. G. He, *J. Am. Chem. Soc.* **2014**, *136*, 14307.
- [4] M. Moses-DeBusk, M. Yoon, L. F. Allard, D. R. Mullins, Z. L. Wu, A. K. Yang, G. Veith, G. M. Stocks, C. K. Narula, *J. Am. Chem. Soc.* **2013**, *135*, 12634.
- [5] L. W. Guo, P. P. Du, X. P. Fu, C. Ma, J. Zeng, R. Si, Y. Y. Huang, C. J. Jia, Y. W. Zhang, C. H. Yan, *Nat. Commun.* **2016**, *7*, 13481.
- [6] P. X. Liu, Y. Zhao, R. X. Qin, S. G. Mo, G. X. Chen, L. Gu, D. M. Chevrier, P. Zhang, Q. Guo, D. D. Zang, B. H. Wu, G. Fu, N. F. Zheng, *Science* **2016**, *352*, 797.
- [7] J. Lin, A. Q. Wang, B. T. Qiao, X. Y. Liu, X. F. Yang, X. D. Wang, J. X. Liang, J. X. Li, J. Y. Liu, T. Zhang, *J. Am. Chem. Soc.* **2013**, *135*, 15314.
- [8] X. J. Zeng, J. L. Shui, X. F. Liu, Q. T. Liu, Y. C. Li, J. X. Shang, L. R. Zheng, R. H. Yu, *Adv. Energy Mater.* **2018**, *8*, 1701345.
- [9] C. H. Choi, M. Kim, H. C. Kwon, S. J. Cho, S. Yun, H. T. Kim, K. J. J. Mayrhofer, H. Kim, M. Choi, *Nat. Commun.* **2016**, *7*, 10922.
- [10] N. C. Cheng, S. Stambula, D. Wang, M. N. Banis, J. Liu, A. Riese, B. W. Xiao, R. Y. Li, T. K. Sham, L. M. Liu, G. A. Botton, X. L. Sun, *Nat. Commun.* **2016**, *7*, 13638.
- [11] X. G. Li, W. T. Bi, L. Zhang, S. Tao, W. S. Chu, Q. Zhang, Y. Luo, C. Z. Wu, Y. Xie, *Adv. Mater.* **2016**, *28*, 2427.
- [12] S. Yang, J. Kim, Y. J. Tak, A. Soon, H. Lee, *Angew. Chem.* **2016**, *128*, 2098; *Angew. Chem., Int. Ed.* **2016**, *55*, 2058.
- [13] H. H. Wei, K. Huang, D. Wang, R. Y. Zhang, B. H. Ge, J. Y. Ma, B. Wen, S. Zhang, Q. Y. Li, M. Lei, C. Zhang, J. Irawan, L. M. Liu, H. Wu, *Nat. Commun.* **2017**, *8*, 1490.
- [14] P. Z. Chen, T. P. Zhou, L. L. Xing, K. Xu, Y. Tong, H. Xie, L. D. Zhang, W. S. Yan, W. S. Chu, C. Z. Wu, Y. Xie, *Angew. Chem.* **2017**, *129*, 625; *Angew. Chem., Int. Ed.* **2017**, *56*, 610.
- [15] L. B. Wang, W. B. Zhang, S. P. Wang, Z. H. Gao, Z. H. Luo, X. Wang, R. Zeng, A. W. Li, H. L. Li, M. L. Wang, X. S. Zheng, J. F. Zhu, W. H. Zhang, C. Ma, R. Si, J. Zeng, *Nat. Commun.* **2016**, *7*, 14036.
- [16] C. Z. Zhu, S. F. Fu, Q. R. Shi, D. Du, Y. H. Lin, *Angew. Chem.* **2017**, *129*, 14132; *Angew. Chem., Int. Ed.* **2017**, *56*, 13944.
- [17] a) J. Kim, C. W. Roh, S. K. Sahoo, S. Yang, J. Bae, J. W. Han, H. Lee, *Adv. Energy Mater.* **2018**, *8*, 1701476; b) H. L. Li, L. B. Wang, Y. Z. Dai, Z. T. Pu, Z. H. Lao, Y. W. Chen, M. L. Wang, X. S. Zheng, J. F. Zhu, W. H. Zhang, R. Si, C. Ma, J. Zeng, *Nat. Nanotechnol.* **2018**, *13*, 411; c) L. Lin, S. Yao, R. Gao, X. Liang, Q. Yu, Y. Deng, J. Liu, M. Peng, Z. Jiang, S. Li, Y.-W. Li, X.-D. Wen, W. Zhou, D. Ma, *Nat. Nanotechnol.* **2019**, *14*, 354.
- [18] a) L. Wei, H. E. Karahan, S. L. Zhai, H. W. Liu, X. C. Chen, Z. Zhou, Y. J. Lei, Z. W. Liu, Y. Chen, *Adv. Mater.* **2017**, *29*, 1701410; b) Y. Z. Jiang, D. Zhang, Y. Li, T. Z. Yuan, N. Bahlawane, C. Liang, W. P. Sun, Y. H. Lu, M. Yan, *Nano Energy* **2014**, *4*, 23; c) W. C. Xu, H. X. Wang, *Chin. J. Catal.* **2017**, *38*, 991.
- [19] a) S. Q. Liu, H. R. Wen, Ying-Guo, Y. W. Zhu, X. Z. Fu, R. Sun, C. P. Wong, *Nano Energy* **2018**, *44*, 7; b) J. S. Yang, J. J. Xu, *Electrochem. Commun.* **2003**, *5*, 306; c) B. R. Goldsmith, B. Peters, J. K. Johnson, B. C. Gates, S. L. Scott, *ACS Catal.* **2017**, *7*, 7543.

- [20] S. Niu, R. McFeron, F. Godinez-Salomon, B. S. Chapman, C. A. Damin, J. B. Tracy, V. Augustyn, C. P. Rhodes, *Chem. Mater.* **2017**, *29*, 7794.
- [21] a) Y. Zhao, L. L. Peng, B. R. Liu, G. H. Yu, *Nano Lett.* **2014**, *14*, 2849; b) P. Z. Chen, K. Xu, X. L. Li, Y. Q. Guo, D. Zhou, J. Y. Zhao, X. J. Wu, C. Z. Wu, Y. Xie, *Chem. Sci.* **2014**, *5*, 2251.
- [22] X. Qin, J. M. Wang, J. Xie, F. Z. Li, L. Wen, X. H. Wang, *Phys. Chem. Chem. Phys.* **2012**, *14*, 2669.
- [23] a) D. Li, J. S. Zhou, X. H. Chen, H. H. Song, *ACS Appl. Mater. Interfaces* **2016**, *8*, 30899; b) Y. Huang, Z. X. Lin, M. B. Zheng, T. H. Wang, J. Z. Yang, F. S. Yuan, X. Y. Lu, L. Liu, D. P. Sun, *J. Power Sources* **2016**, *307*, 649.
- [24] Z. L. Zhang, Y. H. Zhu, H. Asakura, B. Zhang, J. G. Zhang, M. X. Zhou, Y. Han, T. Tanaka, A. Q. Wang, T. Zhang, N. Yan, *Nat. Commun.* **2017**, *8*, 16100.
- [25] D. H. Deng, K. S. Novoselov, Q. Fu, N. F. Zheng, Z. Q. Tian, X. H. Bao, *Nat. Nanotechnol.* **2016**, *11*, 218.
- [26] L. DeRita, J. Resasco, S. Dai, A. Boubnov, H. V. Thang, A. S. Hoffman, I. Ro, G. W. Graham, S. R. Bare, G. Pacchioni, X. Pan, P. Christopher, *Nat. Mater.* **2019**, *18*, 746.
- [27] Y. Zhou, D. E. Doronkin, M. L. Chen, S. Q. Wei, J. D. Grunwaldt, *ACS Catal.* **2016**, *6*, 7799.
- [28] a) P. W. Cai, J. H. Huang, J. X. Chen, Z. H. Wen, *Angew. Chem.* **2017**, *129*, 4936; *Angew. Chem., Int. Ed.* **2017**, *56*, 4858; b) F. C. Lei, Y. F. Sun, K. T. Liu, S. Gao, L. Liang, B. C. Pan, Y. Xie, *J. Am. Chem. Soc.* **2014**, *136*, 6826; c) D. F. Yan, Y. X. Li, J. Huo, R. Chen, L. M. Dai, S. Y. Wang, *Adv. Mater.* **2017**, *29*, 1606459; d) S. H. Ye, Z. X. Shi, J. X. Feng, Y. X. Tong, G. R. Li, *Angew. Chem.* **2018**, *130*, 2702; *Angew. Chem., Int. Ed.* **2018**, *57*, 2672.
- [29] L. Xu, X. C. Xu, L. K. Ouyang, X. J. Yang, W. Mao, J. J. Su, Y. F. Han, *J. Catal.* **2012**, *287*, 114.
- [30] a) K. Liu, A. Q. Wang, T. Zhang, *ACS Catal.* **2012**, *2*, 1165; b) J. Lin, B. T. Qiao, J. Y. Liu, Y. Q. Huang, A. Q. Wang, L. Li, W. S. Zhang, L. F. Allard, X. D. Wang, T. Zhang, *Angew. Chem.* **2012**, *124*, 2974; *Angew. Chem., Int. Ed.* **2012**, *51*, 2920.
- [31] a) J. Bao, X. D. Zhang, B. Fan, J. J. Zhang, M. Zhou, W. L. Yang, X. Hu, H. Wang, B. C. Pan, Y. Xie, *Angew. Chem.* **2015**, *127*, 7507; *Angew. Chem., Int. Ed.* **2015**, *54*, 7399; b) X. D. Zhang, H. X. Li, X. T. Lv, J. C. Xu, Y. X. Wang, C. He, N. Liu, Y. Q. Yang, Y. Wang, *Chem. - Eur. J.* **2018**, *24*, 8822.
- [32] a) E. Tsuji, A. Imanishi, K. Fukui, Y. Nakato, *Electrochim. Acta* **2011**, *56*, 2009; b) D. Z. Wang, Z. P. Wang, C. L. Wang, P. Zhou, Z. Z. Wu, Z. H. Liu, *Electrochem. Commun.* **2013**, *34*, 219; c) D. W. Chen, C. L. Dong, Y. Q. Zou, D. Su, Y. C. Huang, L. Tao, S. Dou, S. H. Shen, S. Y. Wang, *Nanoscale* **2017**, *9*, 11969.
- [33] a) C. C. Chien, J. Z. Shi, T. J. Huang, *Ind. Eng. Chem. Res.* **1997**, *36*, 1544; b) W.-P. Dow, T.-J. Huang, *J. Catal.* **1996**, *160*, 171; c) D. Widmann, R. Leppelt, R. J. Behm, *J. Catal.* **2007**, *251*, 437; d) Z. Y. Pu, X. S. Liu, A. P. Jia, Y. L. Xie, J. Q. Lu, M. F. Luo, *J. Phys. Chem. C* **2008**, *112*, 15045; e) B. Yoon, H. Hakkinen, U. Landman, A. S. Worz, J. M. Antonietti, S. Abbet, K. Judai, U. Heiz, *Science* **2005**, *307*, 403.
- [34] G. Kresse, J. Furthmüller, *Phys. Rev. B* **1996**, *54*, 11169.
- [35] J. P. Perdew, J. A. Chevary, S. H. Vosko, K. A. Jackson, M. R. Pederson, D. J. Singh, C. Fiolhais, **1992**, *46*, 6671.
- [36] G. Kresse, D. Joubert, *Phys. Rev. B* **1999**, *59*, 1758.
- [37] H. J. Monkhorst, J. D. Pack, *Phys. Rev. B* **1976**, *13*, 5188.